

Quantum Interference in Two-Atom Resonant X-ray Scattering of an Intense Attosecond Pulse

Akilesh Venkatesh^{1,*} and Phay J. Ho^{1,†}

¹*Chemical Sciences and Engineering Division, Argonne National Laboratory, Lemont, Illinois 60439, USA*
(Dated: June 13, 2025)

We theoretically investigate resonant x-ray scattering from two non-interacting Ne^+ ions driven by an intense attosecond pulse using a non-relativistic, QED-based time-dependent framework. Our model includes Rabi oscillations, photoionization, Auger decay, and quantum interference among elastic scattering and resonance fluorescence pathways. We analyze how the total scattering signal depends on pulse intensity, atomic configuration, and initial electronic state. We find that the total resonant scattering yield exceeds its non-resonant counterpart; the angular dependence of the signal qualitatively resembles a two-atom structure factor; and the visibility of interference fringes is sensitive to pulse area and the initial electronic state. Only a subset of final states reached via resonance fluorescence exhibits interference, determined by the indistinguishability of photon emission pathways. Fringe visibility is maximized in the linear scattering regime, where ionization is minimal and resonance fluorescence pathways can be largely indistinguishable. These results highlight optimal conditions for applying ultrafast resonant x-ray scattering to single-particle imaging.

I. INTRODUCTION

The ability to extract structural information from x-ray scattering lies at the heart of modern imaging science. Non-resonant elastic scattering, first explained by Bragg over a century ago [1], remains foundational for crystallography by linking interference patterns to periodic atomic structures. Due to its low scattering cross section, non-resonant scattering typically requires crystalline order to achieve sufficient signal. The advent of x-ray free-electron lasers (XFELs) [2–14] has enabled ultrafast studies of matter with atomic spatial and temporal resolution. These sources deliver intense, femtosecond-to-attosecond x-ray pulses [15–18] enabling single-particle imaging (SPI) of isolated systems without requiring crystallization. SPI relies on the principle of “imaging before destruction” [19], where the goal is to capture structural information before radiation-induced ionization and fragmentation degrade the sample.

Yet, even with XFELs, the low cross section of non-resonant scattering necessitates extreme intensities that often trigger rapid ionization and sample destruction [20–26]. To overcome this limitation, resonant scattering from transient ionic states has been explored [27, 28], demonstrating enhanced yield and contrast in xenon clusters [29]. The development of attosecond XFEL pulses [30] with temporal coherence has further advanced SPI by reducing damage and at the same time motivated a study that exploits x-ray-driven Rabi dynamics in neon clusters [31].

The quantum nature of interference underlying resonant scattering has been studied in the optical domain. Richter [32] theoretically predicted first-order interfer-

ence in resonance fluorescence from two non-interacting atoms. Eichmann, Itano and co-workers [33, 34] using a two-ion system as an analog of Young’s double-slit experiment conclusively demonstrated the interference pattern in resonantly scattered light under weak-field monochromatic conditions. They showed that it could be understood through “which-path” arguments [35] that is, the indistinguishability of the scattering pathways which lead to the same final state allows for interference. In the x-ray regime, one-photon interference effects have been theoretically explored under weak-field, monochromatic conditions using perturbative treatments [36–38]. Two-photon interference approaches based on intensity correlations [32, 39, 40] have also been proposed to extract high-resolution structural information from x-ray fluorescence signals [41, 42]. However, questions remain regarding how strong-field ultrafast dynamics, such as Rabi oscillations, photoionization, and Auger decay, modify interference and scattering signatures. In particular, under intense x-ray pulse excitation, both elastic scattering (ES) and resonance fluorescence (RF) pathways can contribute (see Fig. 1), and their interference depends critically on the indistinguishability of the final atomic states.

In prior work [43, 44], we developed a QED-based time-dependent Schrödinger equation (TDSE) framework to model resonant scattering from a single Ne^+ ion under intense ultrafast x-ray pulses. Here, we extend this approach to study coherent scattering from two non-interacting Ne^+ ions, incorporating Rabi dynamics, photoionization, Auger decay, ES, and RF. We analyze how the total scattered signal depends on interatomic separation, geometry, pulse parameters, and initial states. Interference between atoms is shown to encode structural information in the angular distribution, and the total scattered yield under resonant conditions approaches a structure factor form akin to non-resonant diffraction. Fringe visibility is maximum in the linear x-ray scattering

* [avenkatesh\[at\]anl\[dot\]gov](mailto:avenkatesh@anl.gov)

† [pho\[at\]anl\[dot\]gov](mailto:pho[at]anl[dot]gov)

regime, where fluorescence pathways can interfere coherently and ionization is small. These results offer insights about the optimum parameters for using ultrafast resonant scattering in structural imaging.

This paper is organized as follows: We first describe an approach for studying resonant ultrafast x-ray scattering response of two non-interacting atoms in Sec. II. We use the approach to investigate the two-atom scattering response in Sec. III. We present a summary and outlook in Sec. IV. Unless otherwise stated, atomic units are used in the equations presented in this work.

II. METHODS AND MODELLING

We employ a QED-based time-dependent scattering theory approach [45] that was previously used to study the single-atom resonant response [44]. This approach captures processes that involve multiple incident photons but one outgoing photon. In this section, we extend the approach to study the scattering response from two non-interacting atoms of the same kind.

A. Bound state contribution for scattering amplitude

The total vector potential $\hat{\mathbf{A}}$ of the electromagnetic field is written as a sum of a classical incident field \mathbf{A}_C and a quantized outgoing field $\hat{\mathbf{A}}_Q$. The total wavefunction ansatz is,

$$|\psi_{total}(t)\rangle = \psi^{(0)}(t) |0\rangle + \sum_{\mathbf{k}, \epsilon} \psi_{\mathbf{k}, \epsilon}^{(1)}(t) e^{-i\omega_{\mathbf{k}} t} \hat{a}_{\mathbf{k}, \epsilon}^\dagger |0\rangle. \quad (1)$$

Here $\psi^{(0)}$ describes the unscattered wave at the time t and it captures the interaction of the system with the incident classical field. The quantity $\psi_{\mathbf{k}, \epsilon}^{(1)}(t)$ describes the state of the scattered system and the scattering amplitude for a photon to scatter with momentum \mathbf{k} and polarization ϵ .

The incident x-ray field is chosen to be a linearly polarized Gaussian pulse and is described as,

$$\mathbf{A}_C(\mathbf{r}, t) = A_0(\mathbf{r}, t) \sin(\mathbf{k}_{in} \cdot \mathbf{r} - \omega_{in} t) \boldsymbol{\epsilon}_{in}, \quad (2)$$

where \mathbf{r} refers to the position vector. \mathbf{k}_{in} , ω_{in} and $\boldsymbol{\epsilon}_{in}$ are the momentum, energy and polarization of the incident photons, respectively. Also, $\omega_{in} = c|\mathbf{k}_{in}|$, where c is the speed of light in vacuum. The envelope for the Gaussian pulse is,

$$A_0(\mathbf{r}, t) = \frac{E_{in}}{\omega_{in}} \exp\left[\frac{-(2 \ln 2)(t - \frac{\mathbf{k}_{in} \cdot \mathbf{r}}{c})^2}{t_{wid}^2}\right], \quad (3)$$

where E_{in} , and t_{wid} are the incident electric field amplitude and pulse duration (full width half-maximum of the intensity), respectively.

The total Hamiltonian for the system of two identical and non-interacting atoms exposed to an intense attosecond x-ray pulse is,

$$\hat{H}_{tot} = \sum_{j=1}^2 \hat{H}(\mathbf{R}_j) + \sum_{\mathbf{k}, \epsilon} \omega_{\mathbf{k}} \hat{a}_{\mathbf{k}, \epsilon}^\dagger \hat{a}_{\mathbf{k}, \epsilon}. \quad (4)$$

Here \mathbf{R}_j is the position of the j -th atom, each with n_e electrons, and

$$\begin{aligned} \hat{H}(\mathbf{R}_j) = & \sum_{b_j=1}^{n_e} \left[\frac{(\hat{\mathbf{P}}_{b_j} + \hat{\mathbf{A}}(\mathbf{R}_j + \mathbf{r}_{b_j}))^2}{2} + \hat{V}_a(|\mathbf{R}_j - \mathbf{r}_{b_j}|) \right] \\ & + \sum_{i=1, b_j > i}^{n_e} \hat{V}_{ee}(|\mathbf{r}_{b_j} - \mathbf{r}_i|), \end{aligned} \quad (5)$$

where $\hat{\mathbf{P}}_{b_j}$ and $\hat{V}_a(|\mathbf{R}_j - \mathbf{r}_{b_j}|)$ describe the quantum mechanical operator for momentum and for potential energy between the nucleus and the b_j^{th} electron of the j -th atom, respectively. The quantity \hat{V}_{ee} describes electron-electron repulsion within the atom. We neglect the Coulombic interaction and the associated nuclear motion between the two atoms during this scattering process as the time-scale of the nuclear motion is much larger than the pulse duration and the Auger-lifetime of the atoms.

Using the time-dependent Schrödinger equation (TDSE) and following a similar approach to Ref. [44], the equations for $\psi^{(0)}$ and $\psi_{\mathbf{k}, \epsilon}^{(1)}(t)$ are,

$$i \frac{\partial \psi^{(0)}}{\partial t} - \sum_{j=1}^2 \sum_{b_j=1}^{n_e} \hat{H}_C(\mathbf{R}_j + \mathbf{r}_{b_j}, t) \psi^{(0)} = 0, \quad (6)$$

$$i \frac{\partial \psi_{\mathbf{k}, \epsilon}^{(1)}}{\partial t} - \sum_{j=1}^2 \sum_{b_j=1}^{n_e} \hat{H}_C(\mathbf{R}_j + \mathbf{r}_{b_j}, t) \psi_{\mathbf{k}, \epsilon}^{(1)} = \sqrt{\frac{2\pi}{V\omega_{\mathbf{k}}}} e^{i\omega_{\mathbf{k}} t} \sum_{j=1}^2 \sum_{b_j=1}^{n_e} e^{-i\mathbf{k} \cdot (\mathbf{R}_j + \mathbf{r}_{b_j})} \boldsymbol{\epsilon}^* \cdot \left[\hat{\mathbf{P}}_{b_j} + \mathbf{A}_C(\mathbf{R}_j + \mathbf{r}_{b_j}, t) \right] W(t) \psi^{(0)}, \quad (7)$$

where V is the quantization volume, $W(t)$ is a windowing

function that turns on and off adiabatically the interac-

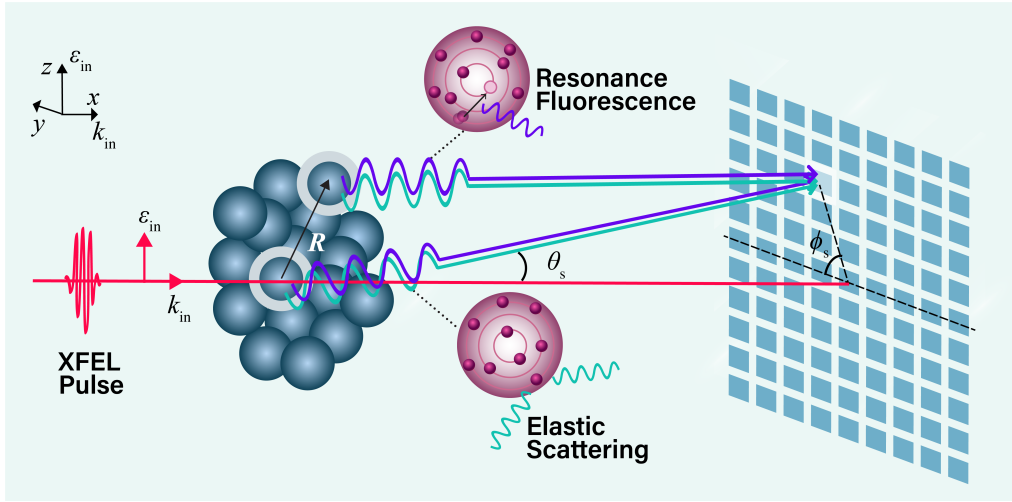


Figure 1: Schematic diagram of resonant scattering from a collection of atoms including both resonance fluorescence and elastic scattering pathways for scattering. The incident x-ray is chosen to be linearly polarized along the z-axis and propagating along the x-axis.

tion with the quantized field, and

$$\hat{H}_C(\mathbf{r}_b, t) = \frac{(\hat{\mathbf{P}}_b + \mathbf{A}_C(\mathbf{r}_b, t))^2}{2} + \hat{V}_a(|\mathbf{r}_b|) + \sum_{i=1, b>i}^{n_e} \hat{V}_{ee}(|\mathbf{r}_b - \mathbf{r}_i|). \quad (8)$$

The combined state of the two non-interacting atoms can be expanded in a basis of tensor product of single-atom eigenstates. Therefore, the expansion of the $\psi^{(0)}$ and $\psi_{\mathbf{k}, \epsilon}^{(1)}(t)$ take the following form,

$$|\psi^{(0)}(t)\rangle = \sum_{m_1, m_2}^{n_s} C_{m_1 m_2}^{(0)}(t) |\psi_{m_1}, \psi_{m_2}\rangle, \quad (9)$$

$$|\psi_{\mathbf{k}, \epsilon}^{(1)}(t)\rangle = \sum_{m_1, m_2}^{n_s} C_{m_1 m_2; \mathbf{k} \epsilon}^{(1)}(t) |\psi_{m_1}, \psi_{m_2}\rangle. \quad (10)$$

$C_{m_1 m_2}^{(0)}$ describes the probability amplitude for the two atoms located at $\mathbf{R}_1, \mathbf{R}_2$ to be in states $|\psi_{m_1}\rangle$ and $|\psi_{m_2}\rangle$, respectively. Here n_s is the number of bound states included for a single atom. Similarly $C_{m_1 m_2; \mathbf{k} \epsilon}^{(1)}(t)$ describes the scattering probability amplitude for the scattered photon to have momentum \mathbf{k} and polarization ϵ and for the two-atom system to be in the state $|\psi_{m_1}, \psi_{m_2}\rangle$.

We proceed similar to the derivation from the single atom response [44] using the the expansion from Eqs. (9) and (10) in Eqs. (6) and (7). Similarly, the effects of Auger decay and photoionization is included in the population but neglected in the scattered states, the equation for $C_{u_1 u_2}^{(0)}(t)$ is,

$$i \frac{\partial C_{u_1 u_2}^{(0)}}{\partial t} - C_{u_1 u_2}^{(0)} (\xi_{u_1} + \xi_{u_2}) - \sum_{m_1, m_2}^{n_s} C_{m_1 m_2}^{(0)} \sum_{j=1}^2 \mathbf{A}_C(\mathbf{R}_j, t) \cdot \langle \psi_{u_j} | \sum_{b_j=1}^{n_e} \hat{\mathbf{P}}_{b_j} | \psi_{m_j} \rangle \prod_{l \neq j} \delta_{u_l m_l} = 0. \quad (11)$$

Here $\delta_{u_l m_l}$ is the Kronecker delta function and $\xi_{u_j} = E_{u_j} - \frac{i}{2} (\Gamma_{a, u_j} + \Gamma_{p, u_j}(t))$. The quantities E_{u_j} , Γ_{a, u_j} and $\Gamma_{p, u_j}(t)$ refer to the binding energy, Auger decay rate and the instantaneous photoionization rate, respectively for the state $|\psi_{u_j}\rangle$. The time-dependent photoionization rate is given by $\Gamma_{p, u_j}(t) = \frac{I(t) \sigma_{u_j}}{\omega_{jn}}$ with σ_{u_j} being the associated one-photon photoionization cross section. To

describe the Rabi dynamics in the atoms, the spatial variation of \mathbf{A}_C is neglected over the size of a single atom [44] consistent with the dipole approximation. However the field experienced by the two separate atoms can be different depending on the choice of \mathbf{R}_j and wavelength, therefore the dependence on \mathbf{R}_j may not be neglected. Importantly, the phase difference between the incident

field arriving at the two atom locations is captured in the \mathbf{R}_j dependence.

$$\begin{aligned}
& i \frac{\partial C_{u_1 u_2; \mathbf{k}\epsilon}^{(1)}}{\partial t} - (E_{u_1} + E_{u_2}) C_{u_1 u_2; \mathbf{k}\epsilon}^{(1)}(t) - \sum_{m_1, m_2} C_{m_1 m_2; \mathbf{k}\epsilon}^{(1)}(t) \sum_{j=1}^2 A_C(\mathbf{R}_j, t) \cdot \langle \psi_{u_j} | \sum_{b_j=1}^{n_e} \hat{P}_{b_j} | \psi_{m_j} \rangle \prod_{l \neq j} \delta_{u_l m_l} \\
& = \sqrt{\frac{2\pi}{V\omega_k}} e^{i\omega_k t} \sum_{m_1, m_2} C_{m_1 m_2}^{(0)}(t) \left[\sum_{j=1}^2 e^{-i\mathbf{k} \cdot \mathbf{R}_j} \boldsymbol{\epsilon}^* \cdot \langle \psi_{u_j} | \sum_{b_j=1}^{n_e} \hat{P}_{b_j} | \psi_{m_j} \rangle \prod_{l \neq j} \delta_{u_l m_l} \right. \\
& \quad \left. - \frac{i}{2} e^{-i\omega_{in} t} \boldsymbol{\epsilon}^* \cdot \boldsymbol{\epsilon}_{in} \sum_{j=1}^2 A_0(\mathbf{R}_j, t) e^{i\mathbf{q} \cdot \mathbf{R}_j} \langle \psi_{u_j} | \sum_{b_j=1}^{n_e} e^{i\mathbf{q} \cdot \mathbf{r}_{b_j}} | \psi_{m_j} \rangle \prod_{l \neq j} \delta_{u_l m_l} \right] W(t).
\end{aligned} \tag{12}$$

Here $\mathbf{q} = \mathbf{k}_{in} - \mathbf{k}$. It is evident from the source terms i.e. the non-homogeneous terms on the right-hand side of Eq. (12), that the first term describe the resonance fluorescence contribution and the last term describe elastic Thomson scattering contribution from all the atoms. For the elastic processes explored in this work, $\omega_k \approx \omega_{in}$ and only those terms from $\langle \psi_{u_j} | \sum_{b_j=1}^{n_e} e^{i\mathbf{q} \cdot \mathbf{r}_{b_j}} | \psi_{m_j} \rangle$ with $u_j = m_j$ contribute. This quantity is the elastic scattering atomic form factor $f_{m_j}(\mathbf{q})$ associated with state m_j . We note that stimulated emission is not included in the scattering probability amplitude calculations. However, stimulated emission produces photons in the same mode of the incident field and can be obtained directly from $\psi^{(0)}$ [44].

The coupled equations for $C_{u_1 u_2}^{(0)}$ and $C_{u_1 u_2; \mathbf{k}\epsilon}^{(1)}$ are solved and $C_{u_1 u_2; \mathbf{k}\epsilon}^{(1)}$ is used for computing the scattering probabilities and differential cross sections [44]. The scattering probability to scatter a photon into angles θ_s , ϕ_s and polarization $\boldsymbol{\epsilon}$ and for the final scattered state to be $|\psi_{m_1}, \psi_{m_2}\rangle$ is $P_{m_1 m_2; \mathbf{k}\epsilon} = |C_{m_1 m_2; \mathbf{k}\epsilon}^{(1)}|^2$. If the final scattered state is not measured, then the scattering probability to scatter a photon with momentum \mathbf{k} and polarization $\boldsymbol{\epsilon}$ is,

$$P_{\mathbf{k}, \boldsymbol{\epsilon}} = \sum_{m_1, m_2} |C_{m_1 m_2; \mathbf{k}\epsilon}^{(1)}|^2. \tag{13}$$

Here, $\mathbf{k} = k(\cos \theta_s, \sin \theta_s \cos \phi_s, \sin \theta_s \sin \phi_s)$ and two allowed choices for outgoing photon polarization are,

$$\begin{aligned}
\boldsymbol{\epsilon}_1 &= (-\sin \theta_s, \cos \theta_s \cos \phi_s, \cos \theta_s \sin \phi_s), \\
\boldsymbol{\epsilon}_2 &= (0, -\sin \phi_s, \cos \phi_s).
\end{aligned} \tag{14}$$

The differential cross section for the two-atom system to scatter a photon into a solid angle $d\Omega$ if its polarization is not measured is given by,

$$\left(\frac{d\sigma}{d\Omega} \right)_B^{(1)} = \frac{V\omega_{in}}{(2\pi)^3} \frac{\int \sum_{\boldsymbol{\epsilon}} P_{\mathbf{k}, \boldsymbol{\epsilon}} k^2 dk}{\int I(t) dt}. \tag{15}$$

The equation for the coefficients $C_{u_1 u_2; \mathbf{k}\epsilon}^{(1)}(t)$ in Eq. (10) is given by,

Here $I(t)$ is the instantaneous incident intensity. One can obtain the differential cross section associated with only ES by turning off the source terms in Eq. (12) associated with RF channel and vice versa [44]. We note that the fluence F of the incident pulse is given by $\int I(t) dt / \omega_{in}$.

While the two-atom calculations are reported for neon, we expect the description of resonant ultrafast x-ray scattering to remain valid for atoms where the dominant decay pathway of the excited state is Auger decay rather than spontaneous emission [44]. While the expressions presented above can in principle be generalized to systems with more than two atoms in bound states, there are several notable challenges. One immediate problem is that, the probability for at least one atom to ionize increases significantly as the number of atoms increases, due to photoionization and Auger decay. When this occurs, the expression derived by only including bound state contribution fails to capture the full photon yield. For systems with more than two atoms, it becomes essential to account for scattering signals arising from configurations where one or more atoms are ionized. The required treatment is nontrivial and beyond the scope of this work.

B. Contribution of Ne^{2+} to scattering probability

The expressions in Sec. II A capture the contribution from configurations in which both atoms remain in bound states. Scattering contributions when one or both atoms are ionized during the pulse, which occurs from photoionization or Auger decay, are not included. In this study where we chose the two initial atoms to be two Ne^+ ions, this would correspond to scattering contribution from further ionized species such as Ne^{2+} (dication) which is not captured in Sec. II A. A rigorous calculation of the scattering signal when one or both Ne^+ ions are further ionized would require the inclusion of all relevant bound states of Ne^{2+} and higher, as well as the continuum states of the ionized electron, in the expansions of Eq.(9) and Eq.(10). However, solving the corresponding

equations is computationally challenging. Here, we use a simplified model to estimate the scattering contribution from Ne^{2+} using the below rate equations [28, 44, 46, 47].

The elastic scattering (ES) contribution from configurations involving dications can be expressed as

$$\begin{aligned} \left(\frac{d\sigma}{d\Omega}\right)_{\bar{d};\text{ES}} &= \frac{1}{\int I(t)dt} \frac{d\sigma_{th}}{d\Omega} \int dt I_{avg}(t) \\ &\times \left\{ \sum_m^{n_s} \left[|\mathcal{F}_{\bar{d}m}(\mathbf{q})|^2 \bar{p}(\mathbf{R}_1, t) p_m(\mathbf{R}_2, t) \right. \right. \\ &+ |\mathcal{F}_{m\bar{d}}(\mathbf{q})|^2 p_m(\mathbf{R}_1, t) \bar{p}(\mathbf{R}_2, t) \\ &\left. \left. + |\mathcal{F}_{\bar{d}\bar{d}}(\mathbf{q})|^2 \bar{p}(\mathbf{R}_1, t) \bar{p}(\mathbf{R}_2, t) \right] \right\}, \end{aligned} \quad (16)$$

where the three terms in curly brackets account for the contributions when atom 1, atom 2, or both atoms are in a dication state (denoted \bar{d}), respectively. I_{avg} is the average of the intensities at the two positions. The structure factors \mathcal{F} are given by

$$\mathcal{F}_{\bar{d}m}(\mathbf{q}) = f_{\bar{d}}(\mathbf{q})e^{i\mathbf{q}\cdot\mathbf{R}_1} + f_m(\mathbf{q})e^{i\mathbf{q}\cdot\mathbf{R}_2}, \quad (17)$$

$$\mathcal{F}_{\bar{d}\bar{d}}(\mathbf{q}) = f_{\bar{d}}(\mathbf{q})e^{i\mathbf{q}\cdot\mathbf{R}_1} + f_{\bar{d}}(\mathbf{q})e^{i\mathbf{q}\cdot\mathbf{R}_2}, \quad (18)$$

where $f_m(\mathbf{q})$ and $f_{\bar{d}}(\mathbf{q})$ are the atomic form factors of Ne^+ in bound state m and Ne^{2+} in its ground state, respectively. In principle, photoionization and Auger decay can populate various dication electronic configurations. However, this approximation is reasonable because the form factors of these configurations are approximately the same at the photon energy considered in this work. The quantity $\bar{p}(\mathbf{R}_j, t)$ denotes the probability of the j -th atom at position \mathbf{R}_j being in a dication state at time t , while $p_m(\mathbf{R}_j, t)$ represents the probability of that atom being in bound state m . The time-dependent Schrödinger equation is solved independently for each atom located at \mathbf{R}_j to obtain its probability amplitude in state m [44]. These are then used to calculate the populations required, such as

$$\bar{p}(\mathbf{R}_L, t) = 1 - \sum_u \left| C_u^{(0)}(\mathbf{R}_L, t) \right|^2, \quad (19)$$

$$p_m(\mathbf{R}_j, t) = \left| C_m^{(0)}(\mathbf{R}_j, t) \right|^2. \quad (20)$$

Also,

$$\frac{d\sigma_{th}}{d\Omega} = r_0^2 (\cos^2 \theta_s \sin^2 \phi_s + \cos^2 \phi_s), \quad (21)$$

is the Thomson differential cross section and r_0 is the classical electron radius. Equation (16) estimates the total ES response as a weighted sum of instantaneous scattering from all electronic configurations, with weights determined by the time-dependent populations and pulse

intensity. This approach is similar in spirit to rate-equation methods [26], but uses TDSE-derived populations for improved accuracy. The presence of the structure factor implies that even ES from partially ionized systems (i.e., with at least one dication) retains interatomic structural information.

Next, we consider the effects of ionization on RF. At least one atom must remain in a bound Ne^+ state [Eq. (9)] to contribute to RF, as the incident x-ray pulse is not resonant with Ne^{2+} . The total fluorescence photon yield for a single atom can be obtained using the rate equation,

$$N_F = \Gamma_{SE} \int p_3(t) dt, \quad (22)$$

where $p_3(t)$ is the time-dependent population of the core-excited state $|3\rangle$, and Γ_{SE} is the spontaneous emission rate. For a single Ne^+ ion, the angular distribution of RF photons is isotropic when polarization is not measured [44]. The RF contribution to the differential cross section from configurations where one atom is a dication and the other is core-excited is,

$$\begin{aligned} \left(\frac{d\sigma}{d\Omega}\right)_{\bar{d};\text{RF}} &= \frac{1}{4\pi} \frac{\omega_{in}}{\int I(t)dt} \Gamma_{SE} \\ &\times \int dt [\bar{p}(\mathbf{R}_1, t) p_3(\mathbf{R}_2, t) + p_3(\mathbf{R}_1, t) \bar{p}(\mathbf{R}_2, t)]. \end{aligned} \quad (23)$$

The total differential cross section for resonant scattering from the two-atom system is then given by the sum of Eqs. (15), (16) and (23),

$$\left(\frac{d\sigma}{d\Omega}\right)_{\text{Tot}} = \left(\frac{d\sigma}{d\Omega}\right)_{\text{B}}^{(1)} + \left(\frac{d\sigma}{d\Omega}\right)_{\bar{d};\text{ES}} + \left(\frac{d\sigma}{d\Omega}\right)_{\bar{d};\text{RF}}. \quad (24)$$

III. RESULTS AND DISCUSSION

In this section, we study the resonant scattering response from two Ne^+ ions, first for the case of intense pulses and then for the case of a low-intensity pulse. The position of first atom \mathbf{R}_1 is located at the origin and the position of the second atom is displaced at \mathbf{R} ($\mathbf{R}_2 = \mathbf{R}$). We use a four-level description for the electronic states (Fig. 2) of each Ne^+ [44], and which include three degenerate states with a vacancy in $2p$ ($1s2p_{-1}^{-1}$, $1s2p_0^{-1}$ and $1s2p_{+1}^{-1}$) and a core-excited state $1s^{-1}2p$. This results in an effective electronic basis of 16 states for the two-atom system. The incident pulse is chosen (see Fig. 1) to have $\hat{\mathbf{k}}_{in} = \hat{x}$, $\boldsymbol{\epsilon}_{in} = \hat{z}$, a pulse duration of 0.25 fs and is resonant with the $1s2p^{-1} \rightarrow 1s^{-1}2p$ core-hole transition with a photon energy of about 849.8 eV. Depending on the incident pulse intensity it can drive Rabi oscillations between $1s2p_0^{-1}$ and $1s^{-1}2p$ in the Ne^+ species, with the pulse area $Q = \int_{-\infty}^{\infty} \Omega(t) dt$. Here $\Omega(t) = \mathbf{E}_{in}(t) \cdot \boldsymbol{\mu}$ is the instantaneous Rabi frequency [48, 49] and $\mathbf{E}_{in}(t)$ and $\boldsymbol{\mu}$ refers to the instantaneous electric field amplitude and

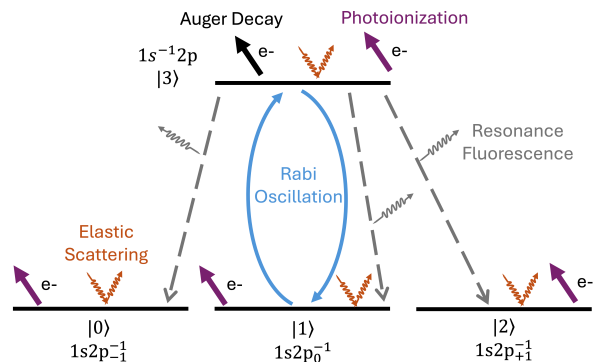


Figure 2: Electronic states of a single Ne^+ . The figure includes photoionization (purple arrow) and Auger decay (black arrows) pathways and electronic transitions associated with Rabi oscillations (blue lines) and resonance fluorescence (gray dashed lines). The elastic scattering processes (orange lines) do not induce electronic transition.

the transition dipole moment. The Ne^+ ions can undergo further ionization through valence photoionization. Also, the core-excited state, which has a lifetime of about 2.4 fs, can undergo Auger decay. The atomic parameters for Ne^+ used are identical to Ref. [44]. The dipole moment for the resonant transition $1s2p_0^{-1} \rightarrow 1s^{-1}2p$ is 0.0524 a.u. [48]. The photoionization cross sections were estimated to be 8.4×10^{-4} a.u. (~ 23.6 kilobarns) and 1.1×10^{-3} a.u. (~ 31.7 kilobarns) for the degenerate ground states and core-hole state, respectively [44, 48]. The atomic form factors of Ne^+ and Ne^{2+} are calculated using Hartree-Fock-Slater electronic structure theory [50].

We numerically solve Eqs. (11) and (12) until there is no dynamics left. This typically involves propagating the equations for much longer than the pulse and until there is no population remaining in the excited states. The actual total time the equations are solved to obtain the coherent resonant response depends on the pulse area and the positions of the atoms. For $Q = 2\pi$ and $Q = \pi$, the propagation times are 209 a.u. and 1588 a.u. respectively.

A. Initial state $|1s2p_0^{-1}, 1s2p_0^{-1}\rangle$

We examine the case when the two Ne^+ ions are both initially in the state with a vacancy in $2p_0$, that is $|\psi_i\rangle = |1s2p_0^{-1}, 1s2p_0^{-1}\rangle$. To explore how scattering yields depend on atomic arrangement, we consider three geometries for the relative orientation vector $\hat{\mathbf{R}} = \hat{x}, \hat{y}, \hat{z}$. In particular, the \hat{y} and \hat{z} cases serve as analogs to Young’s double-slit experiment, with the two Ne^+ ions acting as scattering centers illuminated by an incident coherent x-ray pulse.

We explore two spatial separations, $R = 10\lambda_{in}$ and

$R \rightarrow 0$, where $\lambda_{in} = 2\pi/k_{in}$ is the incident x-ray wavelength. These two limits respectively correspond to cases where the x-ray can and cannot resolve the inter-atomic structure. Additionally, we examine the system’s response under two different pulse intensities corresponding to pulse areas of $Q = 2\pi$ and $Q = \pi$, representing the two extremes of Rabi oscillations. A 2π pulse (intensity $I \sim 2.1 \times 10^{18}$ W/cm²) drives a full Rabi cycle—exciting each Ne^+ ion from $|1\rangle$ to $|3\rangle$ and then back—while a π pulse (intensity $I \sim 5.2 \times 10^{17}$ W/cm²) inverts the population.

1. $Q = 2\pi$ pulse

Figure 3(a) shows the calculated scattering yields for the $Q = 2\pi$ pulse and atomic separation $\mathbf{R} = 10\lambda_{in}\hat{z}$. For simplicity and to restrict the parameter space, we focus on planar scattering where \mathbf{k} , \mathbf{k}_{in} and $\boldsymbol{\epsilon}_{in}$ lie in the same plane (i.e., $\phi_s = 90^\circ$, see Fig. 1). The polarization vector $\boldsymbol{\epsilon}$ of the emitted photon need not lie in this plane. The present calculations involve a sum over final photon polarizations [Eq. (14)].

We first examine the ES yield, shown as orange points in Fig. 3(a). ES originates from any occupied state and does not alter the state of the scatterers. The scattering amplitudes from two identical scatterers contain a phase difference of $e^{i\mathbf{q}\cdot\mathbf{R}}$ [Eq. (12)], giving rise to constructive interference at several θ_s values that satisfy $\mathbf{q}\cdot\mathbf{R} = 2\alpha\pi$ for $\alpha \in \text{Integers}$. This interference arises because an elastically scattered photon emerging from the two atoms in state $|\psi_m, \psi_n\rangle$, cannot be traced to a specific atom here. We compare the calculated ES yield to a fit that is proportional to the structure factor [for example see Eq. (18)] for Thomson scattering from two atoms,

$$g(\theta_s) \propto \frac{d\sigma_{th}}{d\Omega} |f_1(\mathbf{q})|^2 |1 + e^{i\mathbf{q}\cdot\mathbf{R}}|^2, \quad (25)$$

where $|f_1(\mathbf{q})|^2$ is the ES atomic form factor of Ne^+ for the state $1s2p_0^{-1}$ (Sec. II A). For the given incident photon energy, $f_1(\mathbf{q}) \approx f_3(\mathbf{q})$ for all angles. The computed elastic yield matches this fit (Fig. 3(a)), indicating that the ES channel captures the atomic structure consistent with expectations from non-resonant x-ray diffraction.

Next, we examine the RF channel, sometimes referred to as “resonance scattering” [51]. In comparison to ES pathway, the RF pathway has a higher yield and shows similar angular dependence but with a smaller fringe contrast, as shown in Fig. 3(a). For a single atom, the angular dependence of RF is isotropic when the outgoing photon polarization is not measured [44]. However the interference in a small fraction of RF pathways from the two-atom system introduces a slight anisotropy. Due to polarization imposed selection rules, the bound-state population during the pulse is effectively restricted to the $1s2p_0^{-1}$ and $1s^{-1}2p$ states. A single Ne^+ ion emits an RF photon only if it has a nonzero population in its core-hole state $|3\rangle$ (Fig. 2). Thus, the two-atom system emits an

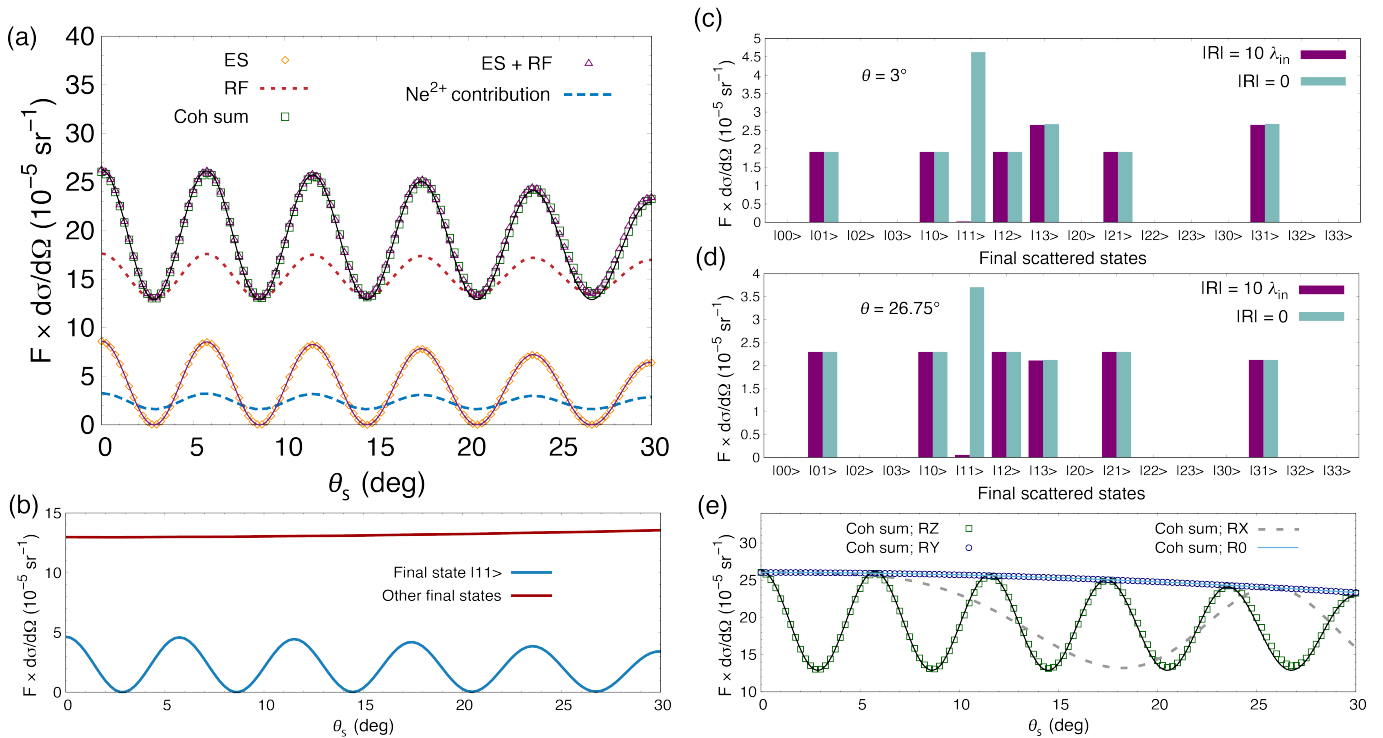


Figure 3: Resonant scattering photon yield from two atoms for a 0.25 fs, $Q = 2\pi$ pulse for the case of planar scattering ($\phi_s = 90^\circ$) when the initial state of each atom is $|1\rangle$. (a) Scattering angle dependence for the two scattering pathways of resonance fluorescence (RF) and elastic scattering (ES), their incoherent sum (ES + RF), coherent sum (Coh sum) and the estimated scattering yields from when one or both of the initial Ne^+ are ionized to Ne^{2+} . The black and purple solid curves are fits [Eq. (25)] which are proportional to the structure factor and $\mathbf{R} = 10\lambda_{in}\hat{z}$. (b) Angle dependence for resonance fluorescence contribution from different final scattered states for the same position of two atoms. (c), (d) Position dependence of resonance fluorescence yields from different final scattered states. (e) Position dependence of the coherent sum. R0, RX, RY and RZ corresponds to $\mathbf{R}=0$, $\mathbf{R} = 10\lambda_{in}\hat{x}$, $\mathbf{R} = 10\lambda_{in}\hat{y}$, and $\mathbf{R} = 10\lambda_{in}\hat{z}$, respectively.

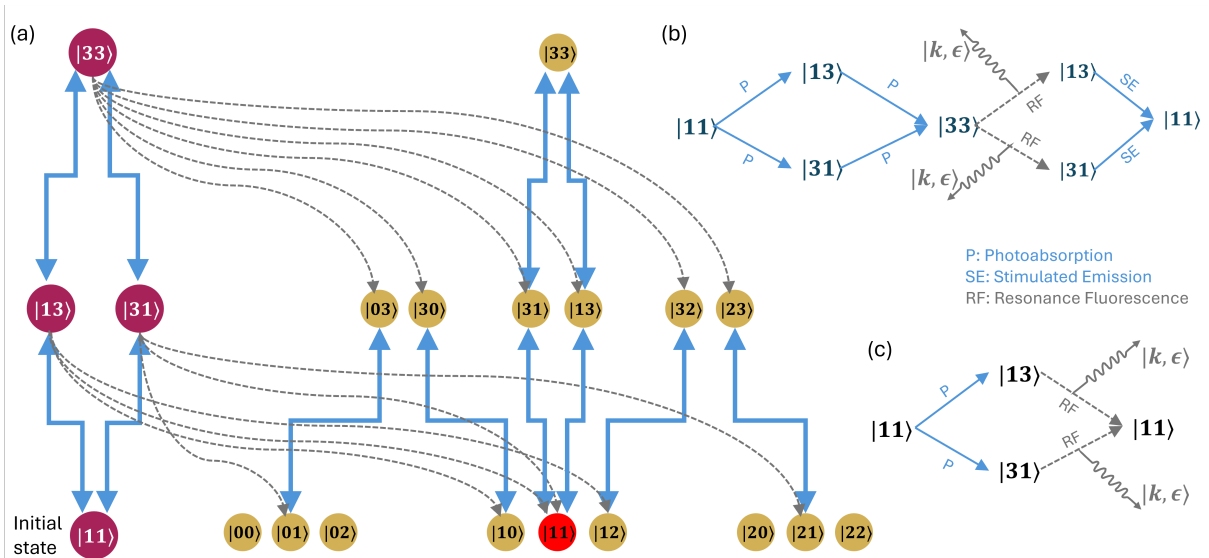


Figure 4: Interference pathways for resonance fluorescence from two atoms when the initial state of the system is $|11\rangle$. (a) The states on the left describe the system before emission (unscattered states, purple circles) and the states on the right describe the scattered electronic states (gold circles) of the system. The blue solid lines and the gray dashed lines depict Rabi oscillation and resonance fluorescence processes respectively. (b), (c) shows two example pathways to obtain a final scattered state $|11\rangle$ (marked red in (a)) for strong and weak incident intensities, respectively.

RF photon when occupying states $\{|13\rangle, |31\rangle, |33\rangle\}$. Depending on \mathbf{k} and ϵ of the RF photon and if further photons are absorbed, the two-atom system may evolve into any of 16 possible final states. These RF pathways are illustrated schematically in Fig. 4. At the beginning of the pulse, the two atom system is in the initial state $|11\rangle$ shown on the bottom-left in Fig. 4 (a). During the pulse, in the absence of RF, one or both atoms can get excited or de-excited during Rabi oscillation shown as blue arrows and states denoted using purple circles. If an RF photon is emitted, the emitting atom transitions to one of the degenerate ground states $|0\rangle, |1\rangle, |2\rangle$ (depicted by gray dashed lines), yielding a set of final states (gold circles) entangled with the outgoing photon. Additional Rabi cycling of these states may follow. Figures 4(b) and 4(c) depict two possible RF interference pathways for the strong- and weak-field cases, respectively.

Fig. 3(b) shows the angular distribution of RF contributions from different final scattered states. Only $|11\rangle$ final scattered state exhibits significant interference fringes resembling those of ES. Figures 3(c) and 3(d) reveal the contribution from each final scattered state for two scattering angles of 3° and 26.75° , corresponding to the interference minima in panel (b) of Fig. 3. These figures confirm that the final scattered state $|11\rangle$ exhibits the strongest position dependence, indicative of significant quantum interference. The $|13\rangle$ and $|31\rangle$ scattered states show a small position dependence as well. Importantly, the limit $\mathbf{R} = 0$ corresponds to the case of maximum constructive interference at any given scattering angle. In contrast, final scattered states involving one atom in $|0\rangle$ or $|2\rangle$ exhibit no dependence on the interatomic separation \mathbf{R} and thus show no interference. This occurs because these states can only be reached through RF if that atom had been excited to the core-hole state $|3\rangle$. Therefore, when an atom ends in $|0\rangle$ or $|2\rangle$, the origin of the photon becomes distinguishable, precluding interference. Among the final states, $|11\rangle, |13\rangle, |31\rangle$, and $|33\rangle$ can each be reached via multiple indistinguishable RF pathways. As a result, they exhibit varying degrees of interference depending on the transition amplitudes of the RF pathways.

Notably, Figs. 3(b)–(d) reveal that the $|11\rangle$ final state can exhibit perfect destructive interference in the RF channel. This occurs only when the emission amplitudes from the two atoms are equal in magnitude and opposite in phase, leading to complete cancellation. Physically, this implies that it is equally probable for either atom to have emitted the RF photon. A conceptual explanation for this behavior lies in the nature of the $Q = 2\pi$ pulse: under such conditions, the system would return to the $|11\rangle$ state even in the absence of fluorescence emission. Hence, if the system ends in $|11\rangle$ after emitting an RF photon, there is intrinsic ambiguity in identifying which atom emitted it, which is an essential requirement for quantum interference.

We note that the final scattered states with at least one atom in $|3\rangle$ predominantly undergo Auger decay (\sim

99% probability) after the pulse ends—a process not explicitly modeled in this work. This is justified for two reasons. First, due to the low scattering cross sections, the probability for an atom to scatter a photon and end up after the pulse in a core-hole state is about 2% or less, making its impact on the population dynamics negligible. Second, after the system has scattered a photon, any subsequent decay process in the scattered states does not change the photon yield.

We now turn to the the total response from both ES and RF channels. Fig. 3(a) shows the angular distribution of the photon yield obtained by retaining all source terms from both channels in Eq.(12), labeled as the “Coh sum”. For comparison, the corresponding incoherent sum is also shown which is defined as the sum of individual channel probabilities, in contrast to the square of the summed amplitudes used in the coherent case. The agreement between the incoherent sum and coherent sum indicates the absence of interference effects in the angular distribution between the two channels for the chosen initial state. This result is consistent with our prior findings for single-atom responses [43, 44]. Interestingly, the angular dependence of the coherent sum closely resembles that of the ES signal, though it is shifted and slightly enhanced. This observation is supported by the agreement with the fitted structure factor function $g(\theta_s)$ [see Eq. (25)], shown as a solid black line in Fig. 3(a), with an appropriate vertical shift applied.

Additional results for three alternative atomic arrangements are presented in Fig. 3(e). For $\mathbf{R} = 10\lambda_{in}\hat{x}$, the different periodicity of the fringes i.e. the distinct scattering angle dependence is a consequence of the different structure factor associated with this arrangement. The case of $\mathbf{R} = 10\lambda_{in}\hat{y}$ does not have any fringes because $\mathbf{q} \cdot \mathbf{R} = 0$ for planar scattering. At small scattering angles, the angular dependence of the coherent sum yield can in principle be used to extract the inter-atomic structure. At large scattering angles, while the fringes remain, the amplitudes of the fringes decreases. Note that the RF channel consists of both interfering pathways and non-interfering pathways. As the scattering angle increases, $\epsilon \cdot \epsilon_{in}$ decreases and hence the contribution from distinguishable final scattered states increases. Therefore the non-interfering part of the RF increases. This non-interfering part of RF has sometimes been referred to as “incoherent component” in some previous works [32, 35].

The coherent sum of ES and RF in Fig. 3 includes only the contribution from the bound states of the system (Sec. II A). When one or both of the initial Ne^+ are further ionized (Sec. II B), the combined contribution from both ES and RF channels (denoted as “ Ne^{2+} contribution”) is shown in Fig. 3(a) for the case of $\mathbf{R} = 10\lambda_{in}\hat{z}$. This contribution displays a small but non-negligible angular dependence, originating from interference in ES between the two species. Qualitatively, this dependence mirrors that seen in the ES channel when both atoms are in one of the bound states. The total scattered photon yield from the two-atom system is therefore given

by the sum of the bound-state contribution and the estimated contribution from including Ne^{2+} , as described in Eq. (24).

2. $Q = \pi$ pulse

Next, we examine the scattering response in a π pulse, as shown in Fig. 5. In the absence of RF, such a pulse would transfer the population from the ground state $|1\rangle$ to the core-hole state $|3\rangle$ at the end of pulse, with some probability for ionization during the pulse. Therefore, as a result, the system produces significant RF after the pulse. The ES channel even though is present during the pulse, its yield is about two orders of magnitude smaller compared to the RF channel. Nonetheless, its angular dependence closely resembles that observed for the $Q = 2\pi$ case. This is supported by agreement using the same fit function of Eq. (25) but with a different proportionality constant. The comparison of Fig. 5 with Fig. 3 shows that the RF signal for $Q = \pi$ displays reduced angular modulation (fringe contrast) relative to the $Q = 2\pi$ case.

As in the $Q = 2\pi$ case, the coherent sum of the ES and RF channel agrees with their incoherent sum as expected. For small-angle scattering, the coherent sum is also found to exhibit qualitatively similar scattering angle dependence to that of ES contribution as evidenced by agreement with a y -shifted fit function. One notable difference observed in Fig. 5(a), is that contribution from the case where at least one or both of the two Ne^+ ions becomes further ionized is substantial relative to the result observed in Fig. 3(a). The reason for this is at the end of the pulse, the entire bound state population is in the core-hole state which results in the entire system to become eventually ionized after the pulse. As one of the two Ne^+ gets ionized first, the other Ne^+ can continue to contribute to the RF channel, until the population in its core-hole state disappears.

Figure 5(b) explains why the RF contribution in Fig. 5(a) only exhibits a small scattering angle dependence. For $Q = \pi$ both atoms get excited and therefore the final scattered states that manifest are those where one of the two excited atoms emits a photon. The final scattered states $|03\rangle, |30\rangle, |23\rangle, |32\rangle$ have no interference as they uniquely identify the emitter. Hence these have no position dependence and this is evident in Fig. 5(c). Additionally, one can understand the maximum interference in the case of $|33\rangle$ using the previous conceptual argument. That is, for the given pulse with $Q = \pi$, each atom (bound part) would have ended up in the final state $|3\rangle$ at the end of the pulse, even if it had not emitted an RF photon. Therefore for the given final scattered state $|33\rangle$, either atom is equally probable to have emitted the RF photon.

Our results suggest that, for a given pulse duration, the intensity of the pulse can be used to control fringe contrasts. It is worth pointing out the dependence of the fringe contrast on the pulse area is analogous to the time-

dependence of the first-order interference effects in RF reported for monochromatic fields by Richter [32]. For imaging applications, given the attosecond time-scale, it can be challenging to develop a time-resolving photon detector. On the other hand, controlling fringe contrast through controlling pulse area by tuning the incident intensity may be a better useful alternative. In addition, the fringe contrasts can also be improved by selecting the polarization of outgoing photons which helps narrow the range of final scattered states to those which allow for interference in RF between two atoms. For example, the final scattered states exhibiting interfering RF pathways are $|11\rangle, |13\rangle, |31\rangle$, and $|33\rangle$. For planar scattering ($\phi_s = 90^\circ$), these arise from outgoing photons with polarization in the scattering plane [Eq. (14)] and when $\epsilon \cdot \epsilon_{in} \neq 0$. The idea of selecting outgoing photon polarization to improve fringe contrast has been experimentally demonstrated for weak-field resonant scattering in optical regime [33, 35].

B. An equal superposition initial state

We investigate the case when the initial state of each Ne^+ ion is an equal superposition of the three degenerate states $|\psi_{sup}\rangle = \frac{1}{\sqrt{3}}[|1s2p_{-1}^{-1}\rangle + |1s2p_0^{-1}\rangle + |1s2p_{+1}^{-1}\rangle]$ for an incident pulse with $Q = 2\pi$. The initial state of the system is given by,

$$|\psi_i\rangle = |\psi_{sup}, \psi_{sup}\rangle \quad (26)$$

In our previous work, for the same pulse condition, the single-atom response of an equal superposition initial state was found to exhibit substantial interference between the ES and RF channels [44] at large scattering angles (θ_s), particularly for azimuthal angle (see Fig. 1) $\phi_s = 135^\circ$ (constructive interference) and $\phi_s = 45^\circ$ (destructive interference).

Figure 6 shows the two-atom resonant scattering response for this initial state [Eq. (26)] for $\phi_s = 135^\circ$ which is 45° off the plane containing \mathbf{k}_{in} and ϵ_{in} . The ES channel displays a similar angular dependence as before, with the interference minimum slightly shifted by $\approx 1^\circ$ due to changes in the momentum transfer vector \mathbf{q} . The overall RF yield is reduced because only one-third of the population in each atom participates in the Rabi dynamics, limiting the maximum core-hole population accordingly. However, the RF angular modulation appears more pronounced than for the initial state $|1s2p_0^{-1}\rangle$ [compare Fig. 6(a) with Fig. 3(a)]. The contribution to the RF yield from different final scattered states, as shown in Fig. 6(b) and Fig. 6(c) for $\theta_s = 4^\circ$ (destructive interference), reveals substantial interference in the RF pathways between the two atoms for several final scattered states. This is expected for these final scattered states, as the initial superposition state [Eq.(26)] prevents one from attributing the emitted RF photon to a specific atom.

Notably, the coherent sum deviates from the incoherent sum at large scattering angles, indicating interference

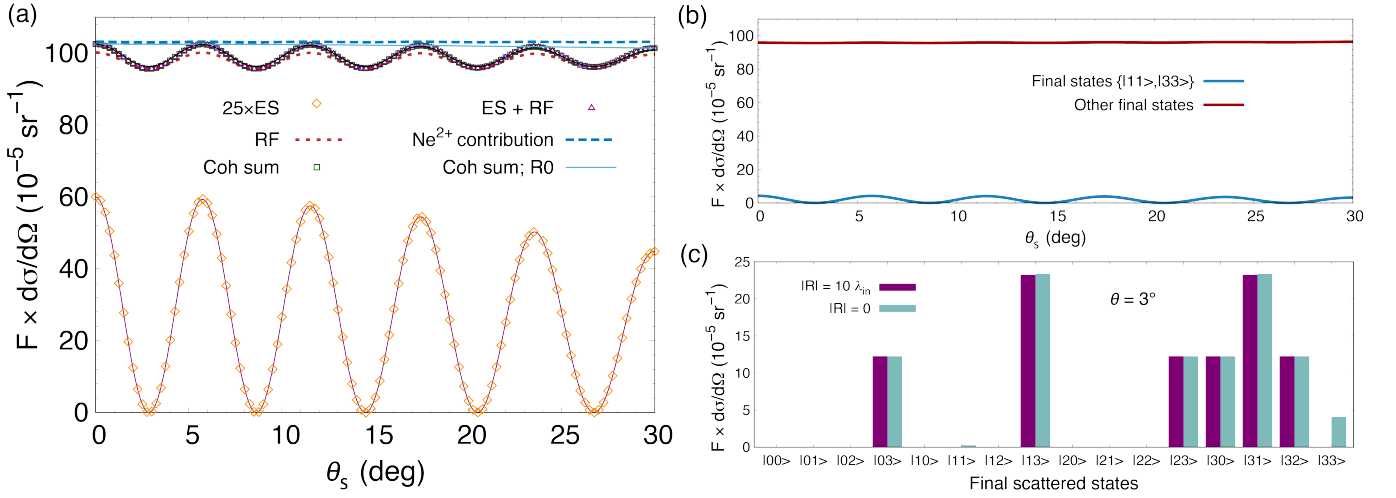


Figure 5: Resonant scattering photon yield from two atoms using a 0.25 fs pulse with $Q = \pi$. (a) Scattering angle dependence from the different channels and an estimated contribution when one or two Ne²⁺ are generated. Note that ES yield is multiplied by a factor of 25 to show its angular dependence. (b) Scattering angle dependence of resonance fluorescence for different final scattered states. (c) Position dependence of resonance fluorescence yields from different final scattered states for $\theta_s = 3^\circ$. The other parameters are the same as Fig. 3.

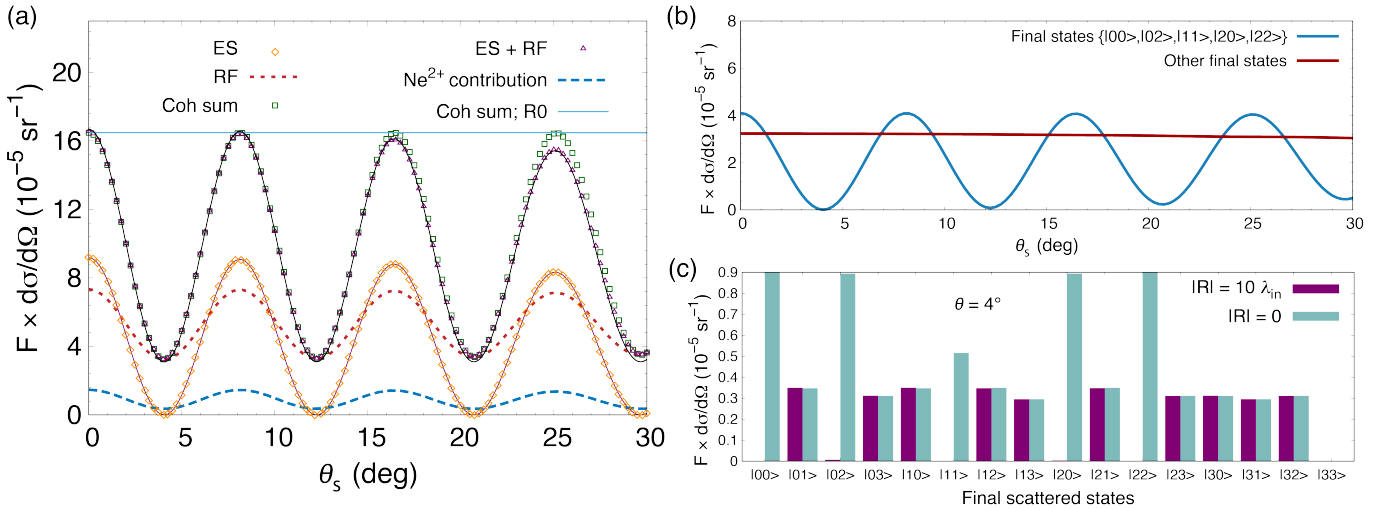


Figure 6: Resonant scattering photon yield from two atoms when both are initially in the same superposition state $|\psi_{sup}\rangle = \frac{1}{\sqrt{3}}(|0\rangle + |1\rangle + |2\rangle)$ [Eq. (26)] and azimuthal angle $\phi_s = 135^\circ$ (out of the plane). (a) Scattering angle dependence for different scattering channels. (b) Resonance fluorescence dependence on scattering angle and final scattered state. (c) Position dependence of resonance fluorescence yields from different final scattered states for $\theta_s = 4^\circ$. The other parameters are the same as Fig. 3.

between the ES channel and RF channels within a single atom, consistent with our previous results [43, 44]. The periodicity (minimum and maximum) of the coherent sum resembles the periodicity in ES, suggesting that the coherent sum still reflects the structure. However, the exact shape of the coherent sum starts to deviate from that of ES yield for large scattering angles.

C. Linear scattering regime

We now examine the resonant x-ray scattering response from the two-atom system exposed to a 0.25-fs pulse of an intensity which corresponds to the linear scattering regime. In this regime, the incident pulse is not intense enough to transfer any significant population from the ground state $1s2p_0^{-1}$ to the core-hole excited state $1s^{-1}2p$ and therefore causes no Rabi cycling. However, the incident pulse can still scatter (both ES and RF)

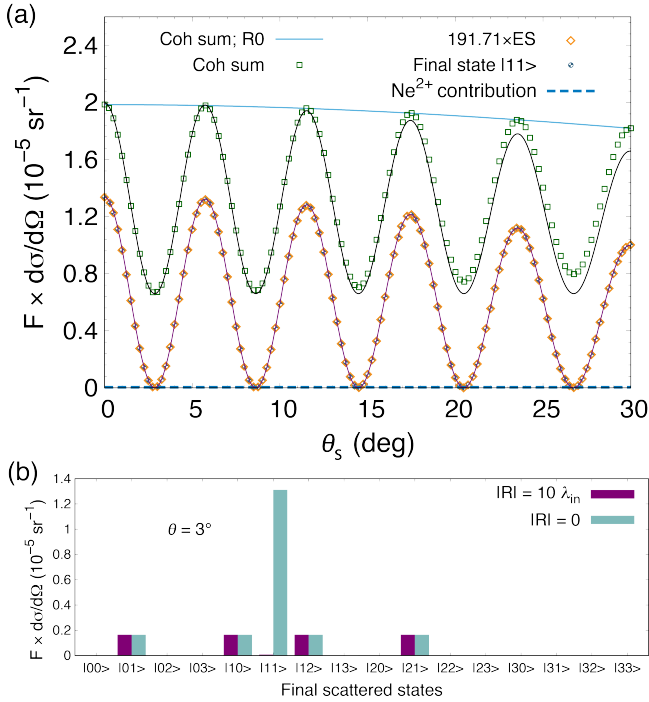


Figure 7: Resonant scattering photon yield from two atoms for a low intensity incident pulse ($Q \sim 0.16$) of duration 0.25 fs. The initial state of each atom is $|1\rangle$. (a) Scattering angle dependence from different channels. The contribution to the photon yield from only resonance fluorescence into the final scattered state $|11\rangle$ is denoted as ‘Final state $|11\rangle$ ’. Note that ES yield is multiplied by a factor of 191.71 to show its angular dependence. (b) Position dependence of resonance fluorescence yields from different final scattered states. The other parameters are the same as Fig. 3.

from the system or photoionize it. For this case, the initial state of the system is chosen to be $|1s2p_0^{-1}, 1s2p_0^{-1}\rangle$.

Figure 7, shows the resulting scattering response for a pulse intensity of about 1.4×10^{15} W/cm², which corresponds to a pulse area of $Q \sim 0.16$. At this intensity, the ES contribution is two orders of magnitude smaller than the RF channel. Therefore, the coherent sum is effectively the same as the RF yield. While the coherent sum exhibits the same angular periodicity as ES, an exact match with ES is only observed at small scattering angles. This deviation is reflected in the mismatch with the shifted fit function $g(\theta_s)$ of Eq. (25).

In this intensity regime, the resonant scattering process can be interpreted as a one-photon in one-photon out process (see Fig. 4(c)). That is, only one of the two atoms is likely to be excited during the pulse, and after emission of an RF photon, the system returns to a final state that does not contain any core-excited population. Depending on the polarization of the outgoing photon, several final scattered states $|01\rangle$, $|10\rangle$, $|11\rangle$, $|12\rangle$, and $|21\rangle$ are accessible. However only the final scattered state $|11\rangle$

exhibits interference, as in this case one cannot determine which of the two atoms scattered the photon [Fig. 7(b)]. The resulting interference pattern from this RF pathway is qualitatively identical to that of the ES channel, as evident in Fig.7(a).

These results suggests that in the linear ultrafast regime, resonant x-ray scattering can reveal the same structural information as conventional non-resonant x-ray scattering, but with a substantially increased yield relative to non-resonant scattering at the same intensity. In addition in this intensity regime, the ionization through photoionization and Auger-decay pathways is found to be negligible and hence the sample damage is minimal.

IV. CONCLUSION AND SUMMARY

In this work, we described a theoretical approach for investigating the resonant x-ray scattering response from two identical non-interacting atoms exposed to an intense attosecond pulse for different intensities, positions of the two atoms, and their initial state. Our calculations showed that while elastic scattering pathways from the two atoms interfere, only a fraction of the resonance fluorescence pathways from the two scatterers can lead to interference. This interference is sensitive to the relative atomic positions and therefore encodes structural information.

Remarkably, we found that the total scattered yield qualitatively reproduces the structure factor known from non-resonant x-ray diffraction. This indicates that resonant x-ray scattering with attosecond pulses, despite being driven by fundamentally different processes, can reveal equivalent interatomic structural features. For the intensities presented, resonant scattering produces a total photon yield that exceeds its non-resonant counterpart by at least a factor of two or more. Both the fringe visibility and the degree of yield enhancement depends strongly on the pulse area and the initial electronic state of the system. A π pulse produces the highest photon yield, but has the lowest fringe visibility. On the other hand, the highest fringe visibility were obtained in linear scattering regime, where ionization is minimal and no Rabi cycling occurs. This regime not only maximizes the ratio of resonant to non-resonant yield for that intensity but also provides optimal structural sensitivity. This finding is consistent with previous predictions made in the context of monochromatic optical fields [32, 52]. However, the photon yield for $Q \sim 0.16$ is about 1 factor of 50 lower than that of a π pulse.

For moderately strong fields associated with few Rabi oscillations, the fringe contrast and the photon yield can be improved by controlling the pulse area (tuning intensity for a given pulse duration). Additional control over the polarization of the outgoing photons can further enhance fringe contrast. Notably, if the two atoms are initially in a superposition state, interference is improved

due to the presence of more indistinguishable RF pathways.

Our results also offer insights into how the ultrafast resonant scattering response scales with system size. In the forward direction, ES signal is expected to scale approximately with the square of the number of atoms, provided ionization remains low, mirroring the scaling behavior familiar from conventional x-ray diffraction. For reference, inelastic processes (such as Compton scattering) are typically incoherent and scale linearly with the number of scatterers. Interestingly, our calculations suggest that under conditions where interference is prominent, the total resonant scattering yield in the forward direction can scale more favorably than linearly, approaching a quadratic dependence in the linear scattering regime.

Overall, these findings highlight the potential of ultrafast resonant x-ray scattering with intense pulses as a structural probe that combines high photon yield with enhanced elemental sensitivity. Since terawatt-scale hard x-ray pulses are now feasible at facilities such as the European XFEL [53], future studies of resonant scattering studies in heavy-element systems using intense attosecond hard x-ray pulse may be insightful. In this regime, inner-shell decay channels are suppressed, valence ionization is less likely, and impact ionization from photoelec-

trons becomes inefficient due to their high kinetic energy. Together, these effects may enable nearly damage-free, element-specific imaging at atomic resolution.

V. ACKNOWLEDGEMENTS

A.V. thanks E. Pelimanni for suggestions about visualization. This work was supported by the U.S. Department of Energy, Office of Basic Energy Sciences, Division of Chemical Sciences, Geosciences, and Biosciences through Argonne National Laboratory. Argonne is a U.S. Department of Energy laboratory managed by UChicago Argonne, LLC, under Contract No. DE-AC02-06CH11357. We gratefully acknowledge the computing resources provided on Improv, a high-performance computing cluster operated by the Laboratory Computing Resource Center at Argonne National Laboratory.

VI. DATA AVAILABILITY

The data plotted in the figures will be openly available upon publication at Ref. [54].

-
- [1] W. H. Bragg and W. L. Bragg, The reflection of x-rays by crystals, *Proceedings of the Royal Society of London. Series A, Containing Papers of a Mathematical and Physical Character* **88**, 428 (1913).
 - [2] P. Emma, R. Akre, J. Arthur, R. Bionta, C. Bostedt, J. Bozek, A. Brachmann, P. Bucksbaum, R. Coffee, F.-J. Decker, *et al.*, First lasing and operation of an ångstrom-wavelength free-electron laser, *Nat. Photon.* **4**, 641 (2010).
 - [3] L. F. DiMauro, J. Arthur, N. Berrah, J. Bozek, J. N. Galayda, and J. Hastings, Progress report on the LCLS XFEL at SLAC, *Journal of Physics: Conference Series* **88**, 012058 (2007).
 - [4] C. Bostedt, S. Boutet, D. M. Fritz, Z. Huang, H. J. Lee, H. T. Lemke, A. Robert, W. F. Schlotter, J. J. Turner, and G. J. Williams, Linac coherent light source: The first five years, *Rev. Mod. Phys.* **88**, 015007 (2016).
 - [5] Z. Huang and K.-J. Kim, Review of x-ray free-electron laser theory, *Phys. Rev. ST Accel. Beams* **10**, 034801 (2007).
 - [6] J. Rossbach, J. R. Schneider, and W. Wurth, 10 years of pioneering X-ray science at the free-electron laser FLASH at DESY, *Physics reports* **808**, 1 (2019).
 - [7] M. Altarelli, The european x-ray free-electron laser facility in hamburg, *Nuclear Instruments and Methods in Physics Research Section B: Beam Interactions with Materials and Atoms* **269**, 2845 (2011), proceedings of the 10th European Conference on Accelerators in Applied Research and Technology (ECAART10).
 - [8] J. Feldhaus, M. Krikunova, M. Meyer, T. Möller, R. Moshhammer, A. Rudenko, T. Tschentscher, and J. Ullrich, AMO science at the FLASH and european XFEL free-electron laser facilities, *Journal of Physics B: Atomic, Molecular and Optical Physics* **46**, 164002 (2013).
 - [9] S. Serkez, G. Geloni, S. Tomin, G. Feng, E. V. Gryzlova, A. N. Grum-Grzhimailo, and M. Meyer, Overview of options for generating high-brightness attosecond x-ray pulses at free-electron lasers and applications at the european XFEL, *Journal of Optics* **20**, 024005 (2018).
 - [10] T. Ishikawa, H. Aoyagi, T. Asaka, Y. Asano, N. Azumi, T. Bizen, H. Ego, K. Fukami, T. Fukui, Y. Furukawa, *et al.*, A compact X-ray free-electron laser emitting in the sub-ångström region, *Nat. Photon.* **6**, 540 (2012).
 - [11] M. Yabashi, Status and perspective on the SACLA facility (Conference Presentation), in *Optics Damage and Materials Processing by EUV/X-ray Radiation VII*, Vol. 11035, edited by L. Juha, S. Bajt, and S. Guizard, International Society for Optics and Photonics (SPIE, 2019).
 - [12] T. Schietinger, M. Pedrozzi, M. Aiba, V. Arsov, S. Bettoni, B. Beutner, M. Calvi, P. Craievich, M. Dehler, F. Frei, *et al.*, Commissioning experience and beam physics measurements at the swissfel injector test facility, *Physical Review Accelerators and Beams* **19**, 100702 (2016).
 - [13] E. Prat, P. Dijkstal, E. Ferrari, and S. Reiche, Demonstration of large bandwidth hard x-ray free-electron laser pulses at swissfel, *Physical review letters* **124**, 074801 (2020).
 - [14] F. Nolting, C. Bostedt, T. Schietinger, and H. Braun, The swiss light source and swissfel at the paul scherrer institute, *The European Physical Journal Plus* **138**, 126 (2023).

- [15] Projected Run 25 LCLS FEL parameters, https://lcls.slac.stanford.edu/sites/default/files/2024-12/LCLS-Parameters-Run-25_0.pdf (2024), accessed: 2025-03-06.
- [16] Instrument specifications, https://www.xfel.eu/facility/instruments/mid/instrument_specifications/index_eng.html (2025), accessed: 2025-03-06.
- [17] M. Yabashi, H. Tanaka, and T. Ishikawa, Overview of the SACLA facility, *Journal of Synchrotron Radiation* **22**, 477 (2015).
- [18] K. Tono, T. Hara, M. Yabashi, and H. Tanaka, Multiple-beamline operation of SACLA, *Journal of Synchrotron Radiation* **26**, 595 (2019).
- [19] R. Neutze, R. Wouts, D. Van der Spoel, E. Weckert, and J. Hajdu, Potential for biomolecular imaging with femtosecond x-ray pulses, *Nature* **406**, 752 (2000).
- [20] L. Young, E. P. Kanter, B. Krässig, Y. Li, A. M. March, S. T. Pratt, R. Santra, S. H. Southworth, N. Rohringer, L. F. DiMauro, G. Doumy, C. A. Roedig, N. Berrah, L. Fang, M. Hoener, P. H. Bucksbaum, J. P. Cryan, S. Ghimire, J. M. Glowina, D. A. Reis, J. D. Bozek, C. Bostedt, and M. Messerschmidt, Femtosecond electronic response of atoms to ultra-intense x-rays, *Nature* **466**, 56 (2010).
- [21] B. Rudek, S.-K. Son, L. Foucar, S. W. Epp, B. Erk, R. Hartmann, M. Adolph, R. Andritschke, A. Aquila, N. Berrah, C. Bostedt, J. Bozek, N. Coppola, F. Filsinger, H. Gorke, T. Gorkhover, H. Graafsma, L. Gumprecht, A. Hartmann, G. Hauser, S. Herrmann, H. Hirsemann, P. Holl, A. Hoemke, L. Journal, C. Kaiser, N. Kimmel, F. Krasniqi, K.-U. Kuehnel, M. Matysek, M. Messerschmidt, D. Miesner, T. Moeller, R. Moshhammer, K. Nagaya, B. Nilsson, G. Potdevin, D. Pietschner, C. Reich, D. Rupp, G. Schaller, I. Schlichting, C. Schmidt, F. Schopper, S. Schorb, C.-D. Schroeter, J. Schulz, M. Simon, H. Soltau, L. Strueder, K. Ueda, G. Weidenspointner, R. Santra, J. Ullrich, A. Rudenko, and D. Rolles, Ultra-efficient ionization of heavy atoms by intense x-ray free-electron laser pulses, *Nat. Photon.* **6**, 858 (2012).
- [22] G. Doumy, C. Roedig, S.-K. Son, C. I. Blaga, A. D. DiChiara, R. Santra, N. Berrah, C. Bostedt, J. D. Bozek, P. H. Bucksbaum, J. P. Cryan, L. Fang, S. Ghimire, J. M. Glowina, M. Hoener, E. P. Kanter, B. Krässig, M. Kuebel, M. Messerschmidt, G. G. Paulus, D. A. Reis, N. Rohringer, L. Young, P. Agostini, and L. F. DiMauro, Nonlinear atomic response to intense ultrashort x rays, *Phys. Rev. Lett.* **106**, 083002 (2011).
- [23] M. Hoener, L. Fang, O. Kornilov, O. Gessner, S. T. Pratt, M. Gühr, E. P. Kanter, C. Blaga, C. Bostedt, J. D. Bozek, P. H. Bucksbaum, C. Buth, M. Chen, R. Coffee, J. Cryan, L. DiMauro, M. Glowina, E. Hosler, E. Kukk, S. R. Leone, B. McFarland, M. Messerschmidt, B. Murphy, V. Petrovic, D. Rolles, and N. Berrah, Ultraintense x-ray induced ionization, dissociation, and frustrated absorption in molecular nitrogen, *Phys. Rev. Lett.* **104**, 253002 (2010).
- [24] S. Schorb, D. Rupp, M. L. Swiggers, R. N. Coffee, M. Messerschmidt, G. Williams, J. D. Bozek, S.-I. Wada, O. Kornilov, T. Möller, and C. Bostedt, Size-dependent ultrafast ionization dynamics of nanoscale samples in intense femtosecond x-ray free-electron-laser pulses, *Phys. Rev. Lett.* **108**, 233401 (2012).
- [25] C. Bostedt, E. Eremina, D. Rupp, M. Adolph, H. Thomas, M. Hoener, A. R. B. de Castro, J. Tiggesbäumker, K.-H. Meiwes-Broer, T. Laarmann, H. Wabnitz, E. Plönjes, R. Treusch, J. R. Schneider, and T. Möller, Ultrafast x-ray scattering of xenon nanoparticles: Imaging transient states of matter, *Phys. Rev. Lett.* **108**, 093401 (2012).
- [26] P. J. Ho, C. Knight, M. Tegze, G. Faigel, C. Bostedt, and L. Young, Atomistic three-dimensional coherent x-ray imaging of nonbiological systems, *Phys. Rev. A* **94**, 063823 (2016).
- [27] E. P. Kanter, B. Krässig, Y. Li, A. M. March, P. Ho, N. Rohringer, R. Santra, S. H. Southworth, L. F. DiMauro, G. Doumy, C. A. Roedig, N. Berrah, L. Fang, M. Hoener, P. H. Bucksbaum, S. Ghimire, D. A. Reis, J. D. Bozek, C. Bostedt, M. Messerschmidt, and L. Young, Unveiling and driving hidden resonances with high-fluence, high-intensity x-ray pulses, *Phys. Rev. Lett.* **107**, 233001 (2011).
- [28] P. J. Ho, B. J. Daurer, M. F. Hantke, J. Bielecki, A. Al Haddad, M. Bucher, G. Doumy, K. R. Ferguson, L. Flückiger, T. Gorkhover, B. Iwan, C. Knight, S. Moeller, T. Osipov, D. Ray, S. H. Southworth, M. Svenda, N. Timneanu, A. Ulmer, P. Walter, J. Hajdu, L. Young, F. R. N. C. Maia, and C. Bostedt, The role of transient resonances for ultra-fast imaging of single sucrose nanoclusters, *Nature Communications* **11**, 167 (2020).
- [29] S. Kuschel, P. J. Ho, A. Al Haddad, F. F. Zimmermann, L. Flueckiger, M. R. Ware, J. Duris, J. P. MacArthur, A. Lutman, M.-F. Lin, *et al.*, Non-linear enhancement of ultrafast x-ray diffraction through transient resonances, *Nature Communications* **16**, 847 (2025).
- [30] J. Duris, S. Li, T. Driver, E. G. Champenois, J. P. MacArthur, A. A. Lutman, Z. Zhang, P. Rosenberger, J. W. Aldrich, R. Coffee, *et al.*, Tunable isolated attosecond x-ray pulses with gigawatt peak power from a free-electron laser, *Nature Photonics* **14**, 30 (2020).
- [31] A. Ulmer, S. Kuschel, B. Langbehn, L. Hecht, S. Dold, L. Rönnebeck, T. Driver, J. Duris, A. Kamalov, X. Li, *et al.*, Exploring damage reduction and scattering cross section enhancement in attosecond x-ray imaging of neon near the k-edge, *Bulletin of the American Physical Society* (2023).
- [32] T. Richter, Interference between the resonance fluorescence fields from two independent atoms and spatial two-photon correlations, *Optics communications* **80**, 285 (1991).
- [33] U. Eichmann, J. C. Bergquist, J. J. Bollinger, J. M. Gilligan, W. M. Itano, D. J. Wineland, and M. G. Raizen, Young's interference experiment with light scattered from two atoms, *Phys. Rev. Lett.* **70**, 2359 (1993).
- [34] W. Itano, U. Eichmann, J. Bergquist, J. Bollinger, J. Gilligan, M. Raizen, and D. Wineland, Light scattered from two atoms, *NIST Technical Note*, 120 (1996).
- [35] W. M. Itano, J. C. Bergquist, J. J. Bollinger, D. J. Wineland, U. Eichmann, and M. Raizen, Complementarity and young's interference fringes from two atoms, *Physical Review A* **57**, 4176 (1998).
- [36] F. K. Gel'mukhanov, L. Mazalov, and N. Shklyueva, An interference effect in x-ray fluorescence spectra, *Zh. Eksp. Teor. Fiz* **69**, 1971 (1975).
- [37] Y. Ma and M. Blume, Interference of fluorescence x rays and coherent excitation of core levels, *Review of scientific*

- instruments **66**, 1543 (1995).
- [38] Y. Ma, X-ray absorption, emission, and resonant inelastic scattering in solids, *Physical Review B* **49**, 5799 (1994).
- [39] R. H. Brown and R. Q. Twiss, Correlation between photons in two coherent beams of light, *Nature* **177**, 27 (1956).
- [40] P. J. Ho, Bringing interferometric imaging into the x-ray regime, *Physics* **16**, 66 (2023).
- [41] A. Classen, K. Ayyer, H. N. Chapman, R. Röhlberger, and J. von Zanthier, Incoherent diffractive imaging via intensity correlations of hard x rays, *Phys. Rev. Lett.* **119**, 053401 (2017).
- [42] P. J. Ho, C. Knight, and L. Young, Fluorescence intensity correlation imaging with high spatial resolution and elemental contrast using intense x-ray pulses, *Structural Dynamics* **8**, 044101 (2021), <https://pubs.aip.org/aca/sdy/article-pdf/doi/10.1063/4.0000105/13835747/044101.1.online.pdf>.
- [43] A. Venkatesh and P. J. Ho, Effect of rabi dynamics in resonant x-ray scattering of intense attosecond pulses, *Physical Review A* **111**, L021101 (2025).
- [44] A. Venkatesh and P. J. Ho, Theory of resonant x-ray scattering with ultrafast intense pulses, *Physical Review A* **111**, 023101 (2025).
- [45] A. Venkatesh and F. Robicheaux, Simulation of nonlinear Compton scattering from bound electrons, *Phys. Rev. A* **101**, 013409 (2020).
- [46] P. J. Ho and R. Santra, Theory of x-ray diffraction from laser-aligned symmetric-top molecules, *Phys. Rev. A* **78**, 053409 (2008).
- [47] J. Cao and K. R. Wilson, Ultrafast x-ray diffraction theory, *The Journal of Physical Chemistry A* **102**, 9523 (1998), <https://doi.org/10.1021/jp982054p>.
- [48] S. M. Cavaletto, C. Buth, Z. Harman, E. P. Kanter, S. H. Southworth, L. Young, and C. H. Keitel, Resonance fluorescence in ultrafast and intense x-ray free-electron-laser pulses, *Phys. Rev. A* **86**, 033402 (2012).
- [49] J. Eberly, Area theorem rederived, *Opt. Express* **2**, 173 (1998).
- [50] P. J. Ho and C. Knight, Large-scale atomistic calculations of clusters in intense x-ray pulses, *Journal of Physics B: Atomic, Molecular and Optical Physics* **50**, 104003 (2017).
- [51] J. Sakurai, *Advanced Quantum Mechanics* (Addison-Wesley Publishing Company, 1967).
- [52] M. Macovei, J. Evers, G.-x. Li, and C. H. Keitel, Strong-field spatial interference in a tailored electromagnetic bath, *Physical review letters* **98**, 043602 (2007).
- [53] J. Yan, W. Qin, Y. Chen, W. Decking, P. Dijkstal, M. Guetg, I. Inoue, N. Kujala, S. Liu, T. Long, *et al.*, Terawatt-attosecond hard x-ray free-electron laser at high repetition rate, *Nature Photonics*, 1 (2024).
- [54] A. Venkatesh and P. J. Ho, Dataset of resonant x-ray scattering of two neon ions exposed to intense attosecond x-ray pulses, [10.5281/zenodo.15604377](https://zenodo.org/record/15604377) (2025).